AIAA JOURNAL
Vol. 37, No. 3, March 1999

Constructing an Entropy-Stable Upwind Scheme for Compressible Fluid Flow Computations

G. F. Naterer*
Lakehead University, Thunder Bay, Ontario P7B 5E1, Canada

A relationship between entropy processes and numerical upwinding is examined in the context of computational gasdynamics. A discretized form of the entropy inequality is constructed at the integration point where convection–diffusion modeling occurs in finite volume methods. Conventional upwinding schemes may violate the local form of the second law of thermodynamics, but a modified upwinding scheme uses additional momentum constraints and pressure terms to provide a positive entropy production rate. The second law is seen as an important quantitative measure of nonphysical numerical results, as well as a sound basis for error analysis. Applications to converging–diverging nozzle and blunt-body flow problems demonstrate the promising performance of the overall numerical algorithm.

Nomenclature

A	= area
a_1, a_2, a_3, a_4	= upwind scheme coefficients
c_p, c_v	= specific heats
D	= diameter
Ec	= Eckert number, $u^2/(c_p \Delta T)$
e	= total energy
F	= entropy flux
$\boldsymbol{f}$	= flux of conserved quantity
L	= length, m, or differential operator
$\dot{m}$	= mass flow rate
$\boldsymbol{n}$	= normal vector
P	= pressure
$\dot{P}_s$	= entropy production rate
q	= conserved quantity
R	= gas constant
S	= entropy
T	= temperature
t	= time
u, v	= velocity components
$\mathcal{V}$	= linearized integration point velocity
x, y	= coordinate directions
α	= weighting factor for hybrid upwind scheme
Γ	= diffusion coefficient
γ	= ratio of specific heats
δ	= discretization error
μ	= dynamic viscosity
ρ	= density
τ	= stress tensor or time integration variable
ϕ	= general scalar

Subscripts

i	= grid point location
ip	= integration point
u	= upstream direction
x, y	= coordinate directions
z	= evaluation at point z
$, z$	= partial derivative with respect to variable z
0	= reference value
1, 2, 3	= local nodes

Superscripts

n	= previous time level
$n+1$	= current time level

Introduction

THE role of generalized entropy in the Euler equations for modern numerical methods is an important concept, but its interpretation in physical terms is difficult. The Euler equations neglect viscous and heat transfer effects; nevertheless, physical entropy production is solely dependent on these processes. However, recent developments have identified and classified two distinct aspects of entropy: 1) natural or physical mechanisms and 2) computational mechanisms. Entropy measures the degree of chaos or randomization, and this disorder can be interpreted in a physical sense (a traditional view) and/or a computational sense (a recent view). The traditional view may be traced to a presentation by the German mathematical physicist Rudolf Clausius in 1850 on the value of entropy in relation to steam engine performance. The recent view has arisen with the advent of digital computers, and it considers entropy in terms of discretization errors, artificial dissipation, and nonphysical numerical results.[1–5]

This recent computational view has included connections between solution uniqueness, numerical stability, overall accuracy, and the second law. For example, Lax[1] implemented a discrete entropy equation to identify physically relevant and unique solutions in finite difference compressible flow simulations. Harten[6] then symmetrized the governing equations through a change of variables (entropy gradient variables) to improve the stability and performance of iterative algebraic solvers. Also, Merriam[3] has shown that satisfaction of the second law is sufficient, in some cases, to ensure stability of compressible flow computations. This numerical stability also suggested that entropy could serve as an effective candidate for solution convergence criteria. In this regard, Camberos[7] has shown that entropy can provide an effective measure of residual error and convergence because it gives a physically significant quantity with a full functional dependence on all fluid state variables. In terms of accuracy, Naterer and Schneider[4] have demonstrated that solution errors and nonphysical phenomena, such as numerical oscillations, often coincide with a violation of the second law within a control volume. In other words, solution accuracy and entropy production are closely related in a numerical sense. Conventional error studies, such as Taylor series expansions, only indicate the behavior of numerical errors as grid refinement is effected. However, in many cases, the mathematical analysis lacks a physical interpretation, and it generally cannot identify errors for coarse grids. Unlike entropy analysis, it also typically cannot identify nonphysical aspects of the numerical results. Thus, unlike Taylor series methods, it appears that the second law can provide a physical basis for

Received July 30, 1997; revision received Oct. 6, 1998; accepted for publication Oct. 26, 1998.

*Assistant Professor, Department of Mechanical Engineering, 955 Oliver Road. Member AIAA.

connections between stability, convergence, reliability, and accuracy of simulations.

During a parallel stage of developments, the first Navier–Stokes solvers appeared with implicit solutions of three-dimensional viscous compressible flows. Important early developments were documented by the MacCormack and Baldwin[8] second-order time-split scheme and the ARC2D and ARC3D codes of Pulliam and Steger.[9] Subsequent advances involved aspects such as boundary-layer and shock-wave interactions, unstructured grids, i.e., finite elements,[10] and conservation-based principles, i.e., finite volumes.[11] However, a great deal of effort and difficulty arose from error analysis and overall generality and robustness of the numerical codes. Solutions were very sensitive to time steps and grid spacing or a variety of empirical constants in the schemes. Rigorous order accuracy often could not be determined. Complicated problems required specialized tuning of coefficients, but the tuning would be altered for each new problem. More grid points and faster computers could achieve more accurate solutions, but they could not necessarily bring a more robust or stable algorithm. In terms of an overall observation, many numerical methods lacked a unified approach to error analysis. Implementation of entropy was absent from these developments. A missing link between error analysis and the earlier generalized entropy studies would soon emerge.

Unified treatments of generalized entropy, finite elements, and viscous compressible flows have appeared in recent studies. Hughes et al.[2] produced finite element schemes that satisfy the second law in a global sense. However, numerical oscillations may occur in individual elements because the second law is not enforced at a local level. Merriam[3] presented a general methodology for satisfying the entropy inequality on a cell-by-cell basis. A general method of analysis rather than a specific finite element or finite volume scheme is presented. Entropy-based corrections for error reduction were implemented for compressible flows by Naterer and Schneider[4] and duct flows by Nellis and Smith.[12] These recent developments improved our understanding of the role of generalized entropy in numerical simulations, but specific studies of the impact on various discretization issues, such as finite volume modeling, remain sparse.

Finite volume methods are commonly employed for compressible flow computations because of their conservation and physically based discretization.[13] The discrete equations are obtained by integration of the governing equations over discrete volumes and approximations of the convection–diffusion terms at the midpoint of the volume surface (integration point). The difficulty with entropy implementation in finite volume schemes is twofold: 1) Conservation laws are equalities, but the second law is an inequality; and 2) discretization occurs at two distinct levels (volume/nodal level and surface/integration point level). Adequate representation of an entropy inequality should be achieved at both nodal and integration point levels. Although extensive research has focused on the accuracy of convection–diffusion modeling, i.e., see Ref. 14, similar investigations of integration point entropy processes have not occurred. In effect, a link between convection–diffusion modeling and entropy-based error analysis has been neglected. Inadequate upwinding accuracy may be related to entropy processes. Momentum and entropy transport at the integration point need to be more closely examined for possible connections in terms of discretization processes and accuracy.

In this paper, a step-by-step process is followed to construct a finite volume scheme that obeys the second law at the integration point. The discretization employs a control-volume-based finite element method. During the development of the entropy discretization, it is observed that the upwinding scheme plays a critical role in the entropy inequality. Conventional upwinding methods are examined in terms of entropy transport, and an entropy-stable approach, or an approach that obeys the local form of the second law, is constructed by a set of momentum transport constraints. The method is then successfully applied to a one-dimensional converging–diverging nozzle problem and a two-dimensional blunt-body flow.

Governing Equations

The governing equations for viscous compressible fluid flow and heat transfer are the Navier–Stokes equations. In the following two-dimensional equations, several assumptions are invoked: 1) laminar flow of an ideal gas, 2) zero source/sink terms, 3) negligible radiative heat transfer, and 4) constant thermophysical properties. In addition, the subsequent entropy analysis considers specific examples, including 1) accelerating flow in a converging nozzle, 2) subsonic converging–diverging nozzle flow, and 3) general duct flows with friction. In these case studies, a steady state is also assumed. The entire numerical scheme is then applied to the converging–diverging nozzle problem for subsonic and supersonic flows, as well as a mixed flow with a shock wave. Finally, its performance in two-dimensional problems is examined by an application to a blunt-body flow simulation.

Let us define a vector of conserved quantities $\boldsymbol{q}$ and a corresponding flux $\boldsymbol{f}$ with an advective component $\boldsymbol{f}^a$ and a pressure p and diffusive component $\boldsymbol{f}^d$:

$$\boldsymbol{q} = \begin{bmatrix} \rho \\ \rho u \\ \rho v \\ \rho e \end{bmatrix}$$

$$\boldsymbol{f} = \begin{bmatrix} \rho u & \rho v \\ \rho uu & \rho uv \\ \rho vu & \rho vv \\ (\rho e + p)u & (\rho e + p)v \end{bmatrix} - \begin{bmatrix} 0 & 0 \\ -p + \tau_{xx} & \tau_{xy} \\ \tau_{yx} & -p + \tau_{yy} \\ u\tau_{xx} + v\tau_{xy} - j_x & u\tau_{xy} + v\tau_{yy} - j_y \end{bmatrix} \tag{1}$$

The heat flux vector $\boldsymbol{j}$ in Eq. (1) can be related to temperature T by Fourier's law.

For each conserved quantity, there exists a corresponding transported scalar ϕ. For example, x momentum is conserved ($q_2 = \rho u$) and the scalar $\phi = u$ is transported by the flow in the momentum transport equation. With this interpretation, the governing equations can then be written in a conservation form as

$$\frac{\partial \boldsymbol{q}}{\partial t} + \nabla \cdot \boldsymbol{f}^a + \nabla \cdot \boldsymbol{f}^d = 0 \tag{2}$$

or a nonconservation transport form (excluding continuity) as

$$\rho \frac{\partial \phi}{\partial t} + \rho \boldsymbol{v} \cdot \nabla \phi + \nabla \cdot \boldsymbol{f}^d = 0 \tag{3}$$

The components of the stress tensor τ in Eq. (1) are

$$\tau_{xx} = 2\mu \frac{\partial u}{\partial x} - \frac{2}{3}\mu \left(\frac{\partial u}{\partial x} + \frac{\partial v}{\partial y} \right) \tag{4}$$

$$\tau_{xy} = \mu \left(\frac{\partial u}{\partial y} + \frac{\partial v}{\partial x} \right) = \tau_{yx} \tag{5}$$

$$\tau_{yy} = 2\mu \frac{\partial v}{\partial y} - \frac{2}{3}\mu \left(\frac{\partial u}{\partial x} + \frac{\partial v}{\partial y} \right) \tag{6}$$

In addition, the ideal gas law, $p = \rho RT$, and the relations $\gamma = c_p/c_v$ and $R = c_p - c_v$, where c_p and c_v refer to specific heats, allow calculations of pressure

$$p = (\gamma - 1)\rho\left(e - \tfrac{1}{2}u^2 - \tfrac{1}{2}v^2\right) \tag{7}$$

Computational Formulation

The problem domain is subdivided into finite elements. For one dimension, Fig. 1a shows the grid structure, and for two dimensions, Fig. 1b shows the appropriate schematic definitions. In one dimension, a control volume is defined by the two adjacent half-elements surrounding each node and the integration points are located at the control volume surfaces. The integration point resides at the element midpoint. Isoparametric, linear-shape functions are used within each element to represent the variation of the dependent scalars in terms

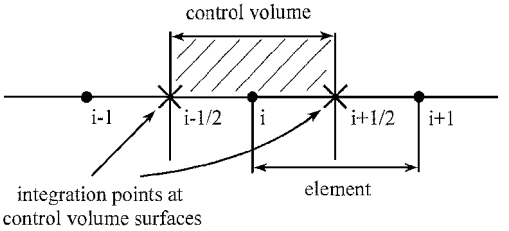

a) One dimensional

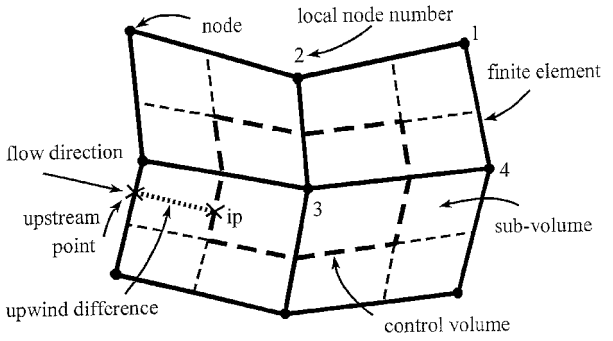

b) Two dimensional

Fig. 1 Grid structures.

of nodal variables. Integrating Eq. (2) over a control volume and time step,

$$\int_V \boldsymbol{q}(t+\Delta t)\,\mathrm{d}V - \int_V \boldsymbol{q}(t)\,\mathrm{d}V + \int_t^{t+\Delta t}\int_S \boldsymbol{f}\cdot\boldsymbol{n}\,\mathrm{d}A\,\mathrm{d}\tau = 0 \quad (8)$$

The discrete equations can be obtained by integration over a specific time interval $t^n \le t \le t^{n+1}$ and also the one-dimensional volume $x_{i-1/2} \le x \le x_{i+1/2}$ for the case of the conservation equations. The discretized conservation and nonconservation forms of the governing equations, Eqs. (2) and (3), respectively, then become in conservation form

$$\frac{\boldsymbol{q}_i^{n+1} - \boldsymbol{q}_i^n}{\Delta t} + \frac{\boldsymbol{f}_{i+1/2} - \boldsymbol{f}_{i-1/2}}{\Delta x_i} = 0 \quad (9)$$

and in nonconservation form

$$\frac{\phi_i^{n+1} - \phi_i^n}{\Delta t} + \frac{1}{\Delta x_i}\sum_{\mathrm{ip}}\left[\dot{m}_{\mathrm{ip}}\phi_{\mathrm{ip}} - \Gamma_{\mathrm{ip}}\left(\frac{\partial\phi}{\partial x}\right)_{\mathrm{ip}}\right] = \text{sources} \quad (10)$$

where sources refers to the remaining terms in the governing equation. The pressure, diffusion, and source terms in Eq. (9) are modeled by linear interpolation and the finite element shape functions. This approach is consistent with the elliptic nature of diffusion and pressure influences. In two dimensions, the advection component differences in Eq. (9) are instead based on upstream differences (Fig. 1b). Diffusion, pressure, and source terms are also handled with a linear interpolation of element nodal values and shape functions. However, in two dimensions, four isoparametric, bilinear shape functions are employed (four nodes per element) rather than the two functions in the one-dimensional case.

To specify a well-posed algebraic system, the advection terms in Eq. (10) at the integration points also need to be related to nodal variables. For these terms, consider the transport of a scalar quantity ϕ across a control volume surface, or integration point, such as $\phi = u$ in the momentum equation. Several approaches have been used in numerical schemes to estimate an integration point value such as $\phi_{i+1/2}$. The following methods represent the current conventional approaches.

Upwind Differencing Scheme

The approximation $\phi_{i+1/2} = \phi_i$ represents an upwind differencing scheme (UDS). In two-dimensional problems, an analogous procedure is the skew upwind differencing scheme (SUDS), which uses the local flow direction to determine the appropriate upstream location for the scalar variable approximation. This first-order upwinding is robust, but it omits the influence of pressure forces on the integration point velocity. It would appear that this omission might create nonphysical solutions. For example, a large pressure gradient in a flowfield would have no direct influence on the integration point velocity, and this anomaly might impose a direct violation of the second law.

Central Differencing Scheme

The central differencing scheme (CDS) uses linear interpolation between adjacent nodal values to find the integration point variable, i.e., $\phi_{i+1/2} = (\phi_i + \phi_{i+1})/2$. This approach yields second-order accuracy. Although CDS improves accuracy, it also produces numerical wiggles and violates the second law with this nonphysical solution behavior, i.e., see Ref. 4.

Hybrid Schemes

Convection models may employ some combination of adjacent nodal values for the integration point approximations. For example, hybrid schemes such as the exponential differencing scheme (EDS) have been developed to provide the correct balance between UDS and CDS influences based on the local grid Peclet number ($Pe = \rho u_i \Delta x_i/\Gamma$) (Ref. 14). The EDS scheme obtains a smooth transition from the CDS scheme for $Pe \to 0$ to the UDS scheme for $Pe \to \infty$. Neglecting transient, pressure, and source terms in Eq. (3) and solving the resulting equation subject to specified values of ϕ at the nodes yields the EDS solution. Evaluating ϕ at the integration point with this EDS solution,

$$\phi_{i+1/2} = [(1+\alpha)/2]\phi_i + [(1-\alpha)/2]\phi_{i+1} \quad (11)$$

where

$$\alpha = 1 - \frac{2(e^{Pe/2} - 1)}{e^{Pe} - 1} \approx \frac{Pe^2}{5 + Pe^2} \quad (12)$$

and the latter approximation is often employed to reduce the computational expense of frequent exponential calculations.[14] Although the correct Peclet number behavior is achieved, this scheme is only first-order in terms of the Taylor series truncation error. Higher-order schemes, such as the quadratic upstream interpolation for convection kinetics (QUICK)[15] scheme, reduce the discretization errors by using quadratic interpolation for integration point values. Also, finite element differential schemes (FIELDS) solve an approximation to the governing equations at the integration point to incorporate the local fluid physics, such as local pressure and source term effects.[16] Although it includes the relevant physical influences, it remains undetermined whether the FIELDS discretization is consistent with the second law.

The objective here is to construct an integration point scheme that will provide entropy-stable solutions. The term *entropy stable* refers to numerical stability, and it has been documented that the second law provides a quantitative measure for ensuring stable computations through the sign of the discretized entropy production rate, i.e., see Ref. 4. Solutions that obey the second law exhibit proper physical characteristics. However, the problem is difficult because the conservation equations are equalities, whereas the second law is an inequality. In the following section, we will examine the role of entropy and how it can be utilized with the current numerical formulation to provide accurate convection–diffusion modeling at the integration point.

Role of Generalized Entropy

A fluid that is governed only by the conservation laws in Eq. (2) could display very unusual behavior because it is not sensitive to the direction of the process required by the second law of thermodynamics. For example, from experience, it is improbable that heated fluid parcels could become sufficiently organized to independently produce a cold fast jet and, therefore, completely convert all thermal energy to kinetic energy. The second law states that the statistical probability of observing this event is very small. Alternatively, the second law states that entropy, which is a property of matter that measures the degree of disorder at the microscopic

level, can be produced but never destroyed in an isolated system. Generalized entropy suggests that these observations also apply to computations, i.e., numerical approximations should not produce nonphysical results.

The second law of thermodynamics can be stated in a form similar to Eq. (2):

$$\dot{P}_s \equiv S_{,t} + \boldsymbol{F}_{,x} \geq 0 \tag{13}$$

where the subscript notation with a comma refers to differentiation. For example, the subscript $,x$ refers to a partial derivative with respect to x in one dimension or the divergence operator in multidimensions. Also, $S(\boldsymbol{q})$ and $\boldsymbol{F}(\boldsymbol{q})$ are the thermodynamic entropy and entropy flux, respectively, where

$$S = \rho s \tag{14}$$

$$F = \rho u s \tag{15}$$

and s is the specific entropy,

$$s = c_v \log\left[\frac{p/p_0}{(\rho/\rho_0)^\gamma}\right] \tag{16}$$

In Eq. (16), the subscript 0 refers to values at a specified initial state. In Eq. (13), the equality refers to reversible processes, and the inequality refers to irreversible processes. Also, Eq. (15) employs a one-dimensional approximation.

For the general case of a simple compressible substance, the entropy and entropy flux must obey two important properties: convexity

$$S_{,\boldsymbol{qq}} < 0 \tag{17}$$

and compatibility

$$S_{,\boldsymbol{q}}\boldsymbol{f}_{,\boldsymbol{q}} = \boldsymbol{F}_{,\boldsymbol{q}} \tag{18}$$

The convexity requirement requires irreversible processes to produce entropy. It ensures that entropy is bounded from above because $S_{,\boldsymbol{qq}}$ must be a negative definite matrix. The entropy distribution typically reaches a maximum value at thermal and mechanical equilibrium. In the compatibility criterion $\boldsymbol{F}_{,\boldsymbol{q}}$ is the entropy flux derivative matrix (a second-order tensor) with a vector component in each of the three coordinate directions. Also, $\boldsymbol{f}_{,\boldsymbol{q}}$ is a third-order tensor because it denotes a derivative of four fluxes in three directions with respect to four conservation variables. The compatibility condition guarantees the existence of an entropy flux satisfying the second law whenever an additional entropy conservation principle holds for reversible processes.

For a discrete volume, the second law can be stated in a form similar to Eq. (9),

$$\dot{P}_s \equiv \frac{S_i^{n+1} - S_i^n}{\Delta t} + \frac{\boldsymbol{F}_{i+1/2} - \boldsymbol{F}_{i-1/2}}{\Delta x_i} \geq 0 \tag{19}$$

After the solution of the conservation equations is obtained, an additional step is required to find $\boldsymbol{q}(\boldsymbol{x}, t)$ from the nodal and integration point values, so that $S(\boldsymbol{q})$ and $\boldsymbol{F}(\boldsymbol{q})$ can be properly integrated. We need to establish an approach that does not violate the second law during this reconstruction step. In this way, if a negative entropy production rate arises, it can be attributed to the discretized conservation equations rather than the entropy inequality, Eq. (19).

We will, therefore, assume that $\boldsymbol{q} = \boldsymbol{q}_i$ within the control volume, where the subscript i refers to node i. This assumption meets the aforementioned requirement because a piecewise constant distribution maximizes the entropy within each control volume with respect to the choice of $\boldsymbol{q}_i$. This can be justified from a fundamental result of thermodynamics, which states that, for all processes at a constant total volume and energy, the entropy increases or remains constant. Thus, when a system is in complete thermal and mechanical equilibrium, i.e., no further processes occur, then its entropy must be a maximum. Because the state transition from $\boldsymbol{q}(\boldsymbol{x}, t)$ to $\boldsymbol{q}_i$ is physically irreversible in general, the entropy contained within an isolated control volume must increase and achieve a maximum value at the equilibrium state $\boldsymbol{q}(\boldsymbol{x}, t) = \boldsymbol{q}_i$. In addition, it will be assumed that $\boldsymbol{q}$ is piecewise constant, at its integration point value, along each control surface.

The calculations of $\boldsymbol{f}$ and $\boldsymbol{q}$ at the integration points in Eq. (9), and thus the entropy flux values in Eq. (19), comprise an important aspect of the scheme's overall accuracy. This aspect of the discretization is called the integration point convection–diffusion modeling or simply the upwinding scheme. The following section outlines the method by which the second law can be directly connected to the discretization of the relevant transport equation at the integration point.

The unique advantage of this second law approach is its potential ability to give an upwind scheme with several desirable features: physically plausible solutions, stable computations, solution uniqueness, efficient convergence properties, etc. A variety of researchers have confirmed that satisfaction of the second law provides a quantitative mechanism to ensure these desirable features. In addition, three examples in the following section will serve to explain the various aspects of the entropy-based model and, thus, give a physical basis for the described desirable features and properties. Conventional schemes, such as upwind or central differencing, are compared from this entropy perspective, and an alternative scheme [physical influence scheme (PINS)] that satisfies the second law is then constructed.

Upwinding and the Second Law

Recall the entropy inequality for control volume i,

$$\dot{P}_s = \frac{S_i^{n+1} - S_i^n}{\Delta t} + \frac{F_{i+1/2} - F_{i-1/2}}{\Delta x_i} \geq 0 \tag{20}$$

The first term may be expanded with a truncated Taylor series:

$$S_i = S_i^n + S_{,t}(t - t^n) + \tfrac{1}{2}S_{,tt}(\eta)(t - t^n)^2 \tag{21}$$

where $t^n \leq \eta \leq t$. Similarly, defining $\boldsymbol{q}_i \leq \zeta \leq \boldsymbol{q}_{i+1/2}$ and expanding the latter term in Eq. (20),

$$F_{i+1/2} = F_i + F_{,\boldsymbol{q}}(\boldsymbol{q}_{i+1/2} - \boldsymbol{q}_i) + \tfrac{1}{2}F_{,\boldsymbol{qq}}(\zeta)(\boldsymbol{q}_{i+1/2} - \boldsymbol{q}_i)^2 \tag{22}$$

If q is a scalar, then the squared term in Eq. (22) represents a scalar multiplication. Otherwise, if $\boldsymbol{q}$ is a vector, then the term is evaluated by the product of the vector and its transpose. In a similar fashion, we can expand the entropy flux about the other integration point:

$$F_{i-1/2} = F_i + F_{,\boldsymbol{q}}(\boldsymbol{q}_{i-1/2} - \boldsymbol{q}_i) + \tfrac{1}{2}F_{,\boldsymbol{qq}}(\zeta)(\boldsymbol{q}_i - \boldsymbol{q}_{i-1/2})^2 \tag{23}$$

Substituting these relations into Eq. (20),

$$\dot{P}_s = \left[S_{,t} + F_{,\boldsymbol{q}}\left(\frac{\boldsymbol{q}_{i+1/2} - \boldsymbol{q}_{i-1/2}}{\Delta x}\right)\right] + \frac{1}{2}\left\{S_{,tt}\Delta t + F_{,\boldsymbol{qq}}\left[\frac{(\boldsymbol{q}_{i+1/2} - \boldsymbol{q}_i)^2 - (\boldsymbol{q}_i - \boldsymbol{q}_{i-1/2})^2}{\Delta x}\right]\right\} \tag{24}$$

Using the compatibility condition and simplifying the first term in Eq. (24),

$$\dot{P}_s = S_{,\boldsymbol{q}}\left[\boldsymbol{q}_{,t} + \boldsymbol{f}_{,\boldsymbol{q}}\left(\frac{\boldsymbol{q}_{i+1/2} - \boldsymbol{q}_{i-1/2}}{\Delta x}\right)\right] + \frac{1}{2}S_{,tt}\Delta t + F_{,\boldsymbol{qq}}\left[\frac{(\boldsymbol{q}_{i+1/2} - \boldsymbol{q}_i)^2 - (\boldsymbol{q}_i - \boldsymbol{q}_{i-1/2})^2}{\Delta x}\right] \tag{25}$$

Although this equation expresses the entropy production rate in terms of several problem variables, it is difficult to implement or verify the positive definite character of individual terms. Instead, we will simplify the first term with another Taylor series:

$$\boldsymbol{q}_{i+1/2} = \boldsymbol{q}_i + \boldsymbol{q}_{,x}(x_{i-1/2} - x_i) + \tfrac{1}{2}\boldsymbol{q}_{,xx}(x_{i+1/2} - x_i)^2 \tag{26}$$

Writing another similar expansion about $x = x_{i-1/2}$ and substituting the results into Eq. (25),

$$\dot{P}_s = S_{,\boldsymbol{q}}(\boldsymbol{q}_{,t} + \boldsymbol{f}_{,x}) + \tfrac{1}{2}S_{,tt}\Delta t \geq 0 \tag{27}$$

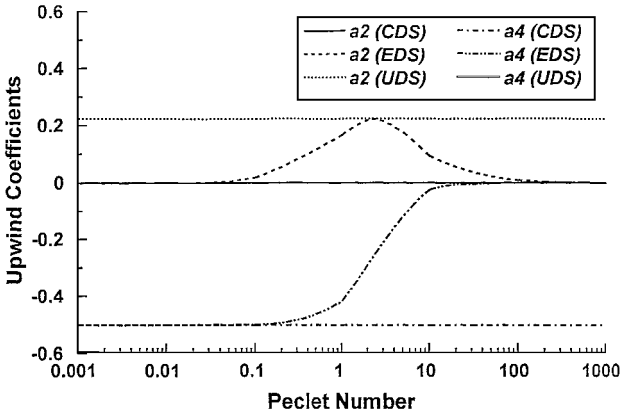

Fig. 2a Conventional upwind coefficients.

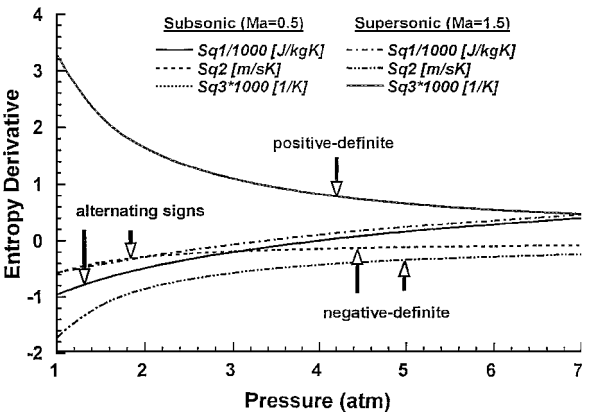

Fig. 2b Rate of entropy change. (Note: *Sq*3 subsonic and *Sq*3 supersonic results are coincident along the upper positive-definite curve.)

The row vector $S_{,\boldsymbol{q}}$ in Eq. (27) represents a rate of change of entropy with respect to a specific conserved quantity. If the conservation equations are solved in an exact fashion, then the first term in Eq. (27) vanishes and the second term remains positive to satisfy the entropy inequality. Note that Eq. (27) remains valid at both the control volume level, where the overall conservation equations are applied, and the integration point level, where assumptions regarding convecting quantities, such as $\phi_{i+1/2} = \phi_i$ (UDS scheme), are employed. In the latter case, violation of the inequality in Eq. (27) may lead to observed errors, such as false diffusion in the case of UDS or oscillations in the case of CDS. Thus, the convection modeling at the integration points should be governed by the same entropy requirements as the overall conservation equation.

Using the nonconservation transport form of the governing equations, Eq. (3), and writing the bracketed component of the first term in Eq. (27) in its discretized form at $x = x_{i+1/2}$,

$$L(\tilde{\boldsymbol{q}}) + \delta = a_1\rho\left(\frac{\phi^{n+1} - \phi^n}{\Delta t}\right) + a_2\rho u\left(\frac{\phi_{i+1/2} - \phi_i}{\Delta x_i/2}\right) + a_3\left(\frac{P_{i+1/2} - P_i}{\Delta x_i/2}\right) + a_4\Gamma\left(\frac{\phi_{i+1} - 2\phi_{i+1/2} + \phi_i}{\Delta x_i^2}\right) \tag{28}$$

In this form, the exact equation $L(\boldsymbol{q}) = 0$, Eq. (3), is replaced by a discrete approximation, $L(\tilde{\boldsymbol{q}}) + \delta = 0$, where $L()$ refers to the differential operator (left-hand side) in Eq. (3) and δ refers to discretization errors at $x_{i+1/2}$. We know that $\delta \to 0$ as grid and time step refinement is effected.

Upon close examination of Eq. (28), we notice that it represents a series of conventional models for integration point approximations: 1) CDS for $a_1 = a_2 = a_3 = \delta = 0$ and $a_4 \neq 0$, 2) UDS for $a_1 = a_3 = a_4 = \delta = 0$ and $a_2 \neq 0$, and 3) EDS for $a_1 = a_3 = \delta = 0$, $a_2 = \alpha/Pe$, and $a_4 = (1-\alpha)/2$.

Figure 2a shows these coefficients and their dependence on Pe. As $Pe \to \infty$, it can be shown from Eq. (28) that $|a_4| \ll |a_2|$, and thus, the UDS upstream values dominate the downstream influences even though a_2 becomes small. The difficulty now is to determine whether these coefficients violate the entropy inequality in Eq. (27).

The first term after the equality in Eq. (27) represents a product between each component of the row vector $S_{,\boldsymbol{q}}$ and a conservation (or transport) equation represented by each component of a column vector, i.e., $S_{,q_1}$ (continuity) + $S_{,q_2}$ (momentum transport equation) + $S_{,q_3}$ (energy transport equation). The numerical entropy production of each individual contribution should be high enough to prevent an overall negative sum and a violation of Eq. (27). The effect of a particular transport equation, such as the momentum transport equation, can be examined by assuming that the remaining transport equations closely approximate their exact solutions, and thus their contributions to the aforementioned vector product are negligible. In addition, let us consider steady-state problems ($a_1 = 0$). We can then assemble individual terms and examine their signs.

To clarify the results, let us consider the physical interpretation of individual terms in the entropy analysis for the following three examples. These examples include interpretations for an accelerating flow in a converging nozzle, converging–diverging nozzle flow, and other general duct flows with friction.

Example 1: Interpretation for Accelerating Flow in a Converging Nozzle

Recall that the row vector $S_{,\boldsymbol{q}}$ in Eq. (17) refers to a rate of change of entropy with respect to a conserved quantity. For example, if the x momentum ($q_2 = \rho u$) increases by an incremental amount $\mathrm{d}q_2$, where d refers to differential, as a flow accelerates through a converging nozzle, then the term $S_{,q_2}\,\mathrm{d}q_2$ represents the associated entropy increase. The term $S_{\boldsymbol{q}}\,\mathrm{d}\boldsymbol{q}$ would represent the cumulative effect of changes in all conserved quantities on the entropy change. From Eqs. (1), (7), (14), and (16), we can calculate this entropy derivative:

$$S_{,\boldsymbol{q}} = \left\{ s + c_v\left[-\gamma + \frac{(\gamma-1)\rho u^2}{2P}\right], -c_v\frac{(\gamma-1)\rho u}{P}, \rho c_v\frac{(\gamma-1)}{P} \right\} \tag{29}$$

The components of $S_{,\boldsymbol{q}}$ in Eq. (29) are shown in Fig. 2b for the case of air with $\gamma = 1.4$, $T = 300$ K, $\rho = 1.16$ kg/m^3, $c_v = 717.4$ J/kgK, and $p_0 = 101$ kPa. In Eq. (29), we can observe that, for one-dimensional flows from left to right, the sign of $S_{,q_1}$ may be positive or negative but $S_{,q_2} \leq 0$ and $S_{,q_3} \geq 0$. These properties can be observed in Fig. 2b. In physical terms, for the earlier nozzle example, this implies that the entropy would decrease with a positive change $\mathrm{d}q_2$ because there would be more certainty with the whereabouts of a fluid parcel in the converging duct. In Fig. 2b, it can be seen that this uncertainty principle also affects the magnitude of the entropy change; $|S_{,q_2}|$ for supersonic flow is larger than the corresponding subsonic value at a fixed pressure. On the other hand, the entropy increases with a positive change in $\mathrm{d}q_3$ because the higher degree of molecular disorder associated with the increased thermal energy implies that its entropy must also increase.

Example 2: Interpretation for Subsonic Converging–Diverging Nozzle Flow

From Eqs. (28) and (29), we can construct the entropy production rate associated with momentum discretization,

$$(S_{,\boldsymbol{q}}\boldsymbol{f}_{,x})_2 = \frac{-c_v(\gamma-1)\rho u}{P}\left[a_2\rho\bar{u}\left(\frac{u_{i+1/2} - u_i}{\Delta x_i/2}\right) + a_3\left(\frac{P_{i+1/2} - P_i}{\Delta x_i/2}\right) + a_4\Gamma\left(\frac{u_{i+1} - 2u_{i+1/2} + u_i}{\Delta x_i^2}\right)\right] \tag{30}$$

Equation (30) demonstrates a set of necessary constraints on conventional upwind schemes to satisfy the entropy inequality. For example, consider an accelerating flow in a subsonic converging–diverging nozzle, i.e., $\partial u/\partial x > 0$, just upstream of the throat. If the

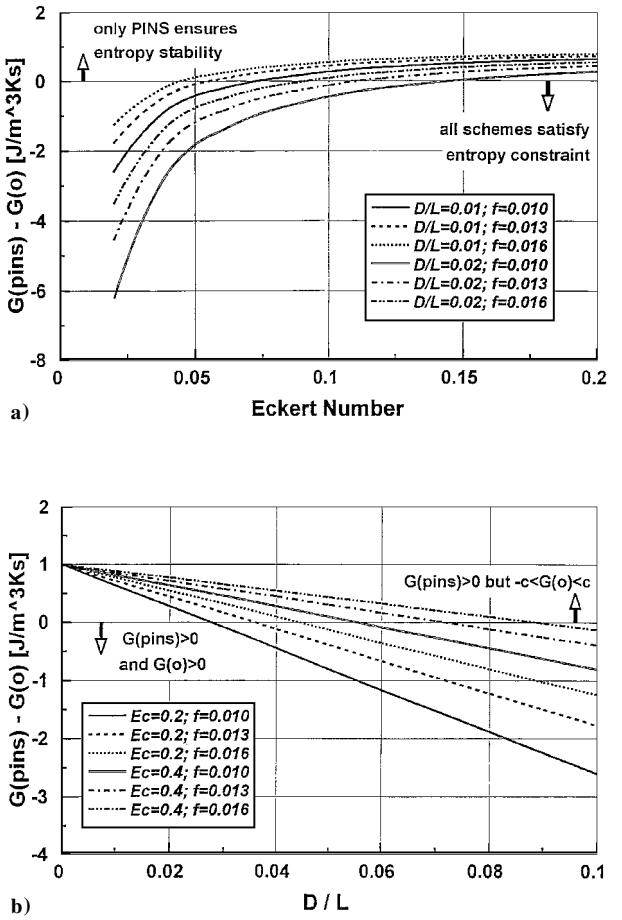

Fig. 3 Regions that satisfy the entropy constraint in terms of a) *Ec* and b) *D/L* sensitivity.

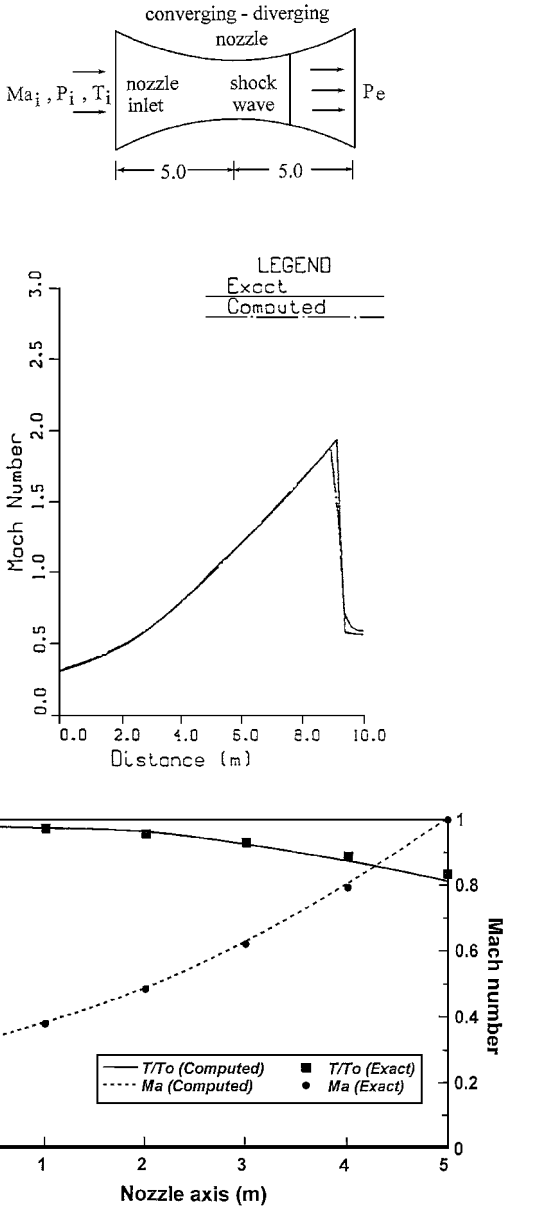

Fig. 4 Converging–diverging nozzle: a) schematic with geometry and numerical results for examples with b) shock wave and c) supersonic flow.

flow remains subsonic, then it will begin to decelerate upstream of the throat due to the upcoming area expansion in the duct. As a result, the concavity of the velocity profile changes in the region upstream of the throat from concave upward to concave downward, or, in other words, a convex profile exists upstream of the throat. Under these conditions with CDS, UDS, SUDS, or EDS schemes ($a_3 = 0$), we notice that $S_{,q}\boldsymbol{f}_{,x} < 0$ in Eq. (30) and the entropy inequality in Eq. (27) is violated. In practice, viscous terms are negligible outside of the boundary layer in this case; nevertheless, Eq. (30) remains negative for accelerating flows, and thus we must modify the upwinding to prevent negative entropy production. For example, the schemes may apply the approximation to decelerating flows instead or modify the upwinding with additional terms.

Let us construct an upwind scheme by imposing a momentum constraint on the pressure terms in Eq. (30) to satisfy Eq. (27). An appropriate pressure influence at the integration point may prevent the problem in the aforementioned example with an accelerating flow. For steady flow, Bernoulli's equation can be written in the following form[17]:

$$P_i + \rho\frac{u_i^2}{2} = P_{i+1/2} + \rho\frac{u_{i+1/2}^2}{2} + \text{losses} \tag{31}$$

where losses ≥ 0 represent frictional losses. Notice that the velocity terms in Eq. (31) may be factored in the following form:

$$P_i - P_{i+1/2} + \rho\bar{u}(u_i - u_{i+1/2}) = \text{losses} \tag{32}$$

where $\bar{u} = (u_i + u_{i+1/2})/2$. It is now evident from Eqs. (30) and (32) that, if we set $a_2 = a_3$ for PINS and $a_4 \approx 0$ (negligible downstream influences for high Peclet number case), then the losses may be isolated, and Eq. (30) may be rewritten as follows:

$$(S_{,q}\boldsymbol{f}_{,x})_2 = 2\frac{a_2 c_v(\gamma-1)\rho u}{\Delta x_i P}(\text{losses}) \geq 0 \tag{33}$$

The second law requirement in Eq. (27) is now satisfied by the proposed PINS scheme. In addition, it can be shown that this scheme exhibits second-order accuracy (see Appendix).

Example 3: Interpretation for General Duct Flows with Friction

A detailed comparison between the PINS scheme and other conventional schemes (subscript o), such as CDS, UDS, SUDS, and EDS schemes, will now be examined and interpreted in the context of general duct flows with friction. Recall the definition of the wall shear stress, $\tau_w = f\rho u^2/2$, for incompressible flows, where f refers to the friction factor. This definition shows good agreement with experimental data for incompressible flows, as well as subsonic compressible flows[17]; experimental data for supersonic and hypersonic flows are sparse. Defining $G = (S_{,q}\boldsymbol{f}_{,x})_2$ and $Ec = u^2/c_p\Delta T$ (Eckert number), then the difference between upwind schemes can be computed using the ideal gas law with the following result:

$$G_{\text{PINS}} - G_o = 2\frac{a_{2,o}c_v(\gamma-1)\rho u}{\Delta x_i P}\left[\frac{a_{2,\text{PINS}}}{a_{2,o}} - 1 - \frac{2(\gamma-1)}{\gamma}\left(\frac{D}{L}\right)\left(\frac{1}{fEc}\right)\right](\text{losses}) \tag{34}$$

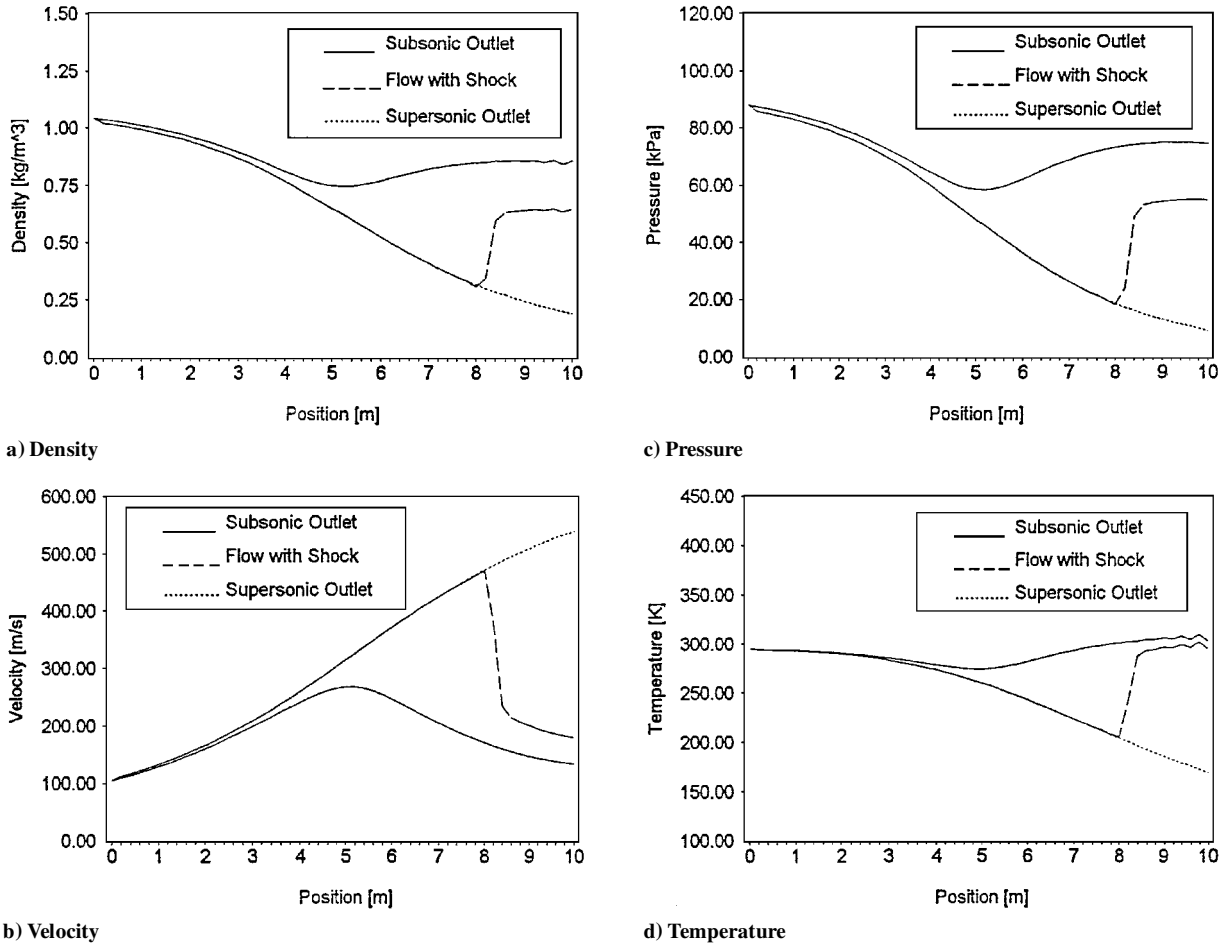

Fig. 5 Results of converging–diverging nozzle.

The critical points, $\tilde{E}c$ and $\tilde{D}/L$, where this difference changes signs can be readily computed:

$$\tilde{E}c = \frac{2(\gamma-1)}{\gamma f}\left(\frac{D}{L}\right)\left(\frac{a_{2,o}}{a_{2,\text{PINS}} - a_{2,o}}\right)$$

$$\left(\frac{\tilde{D}}{L}\right) = \left(\frac{a_{2,\text{PINS}}}{a_{2,o}} - 1\right)\frac{\gamma}{2(\gamma-1)} f Ec \tag{35}$$

Thus, conventional schemes are guaranteed to exhibit entropy-stable behavior only for low Eckert numbers below the critical points. These trends are shown in Fig. 3, where the following sample constants have been selected: $\gamma = 1.4$ (air), $a_{2,\text{PINS}} = a_{3,\text{PINS}} = 1$, and $P_i \equiv c_v(\gamma-1)\rho u_i(\text{losses})(a_{2,\text{PINS}} - a_{2,o})/\Delta x_i$. Below the critical points, $G_{\text{PINS}} < G_o$, but $G_{\text{PINS}} \geq 0$ for all Eckert numbers, and thus $G_o \geq 0$ is guaranteed also in this region. However, above the critical points, the PINS scheme satisfies the entropy inequality in Eq. (27), but the other schemes may violate it. Both Figs. 3a and 3b show that the difference $G_{\text{PINS}} - G_o$ increases with the friction factor at a specific Ec or diameter/length D/L ratio, respectively, because higher wall friction produces more entropy for a pressure-weighted scheme than a scheme, such as UDS, without this dependence. Friction, pressure loss, and entropy production are, thus, closely related to the integration point approximations.

Because the current analysis considers only the momentum transport discretization aspects of Eq. (27), the overall accuracy or numerical stability of a specific finite volume method is not formally established. However, each integration point discretization is generally constructed independently of the other transport equations. Thus, if nonmomentum aspects are considered equivalent, then the present studies show that the PINS scheme is the only assured entropy-stable approach. The results in the following section will demonstrate the performance of the PINS upwind scheme and the overall numerical formulation.

Application Problems and Discussion

The performance of the numerical model for compressible flow computations will now be examined by applications to two example problems: 1) a converging–diverging nozzle problem and 2) a two-dimensional blunt-body impingement problem.

Converging–Diverging Nozzle Problem

In the following example, a compressible fluid (air) flows through a converging–diverging nozzle with a specified cross-sectional area $A(x)$:

$$A(x) = A_{\text{th}} + (A_e - A_{\text{th}})[1 - (x/5)]^2, \qquad x \leq 5 \tag{36}$$

$$A(x) = A_{\text{th}} + (A_e - A_{\text{th}})[(x/5) - 1]^2, \qquad x \geq 5 \tag{37}$$

where $0 \leq x \leq 10$ m and A_{th} and A_e are the throat and exit areas ($A_e = 2.035A_{\text{th}}$; see Fig. 4a). Gas properties for air include $\gamma = 1.4$, $c_p = 1004$ J/kgK, and $R = 287$ J/kgK.

In this problem, stagnation pressure ($P_0 = 93.75$ kPa) and temperature ($T_0 = 300$ K) conditions, as well as the inlet Mach number ($Ma_i = 0.3$), are specified. The inlet conditions are also used as the initial conditions throughout the problem domain. Zero fluid-penetration conditions are defined along the nozzle walls. Uniform node spacing in the transverse and axial directions with 2×50 elements was employed. Computer simulations were conducted by marching ahead in time ($\Delta t = 0.1$ms) from the initial conditions to the final steady-state solution. Approximately 800 iterations (or time steps) were typically required to achieve the final steady state. In addition, up to 1500 additional iterations were performed after the steady state to confirm the stability of the results and to verify that specific aspects, such as shock-wave location, did not change.

Three different back pressures are specified, and these three values produce the following conditions in the diverging section of the nozzle: 1) subsonic flow ($P_e = 80$ kPa), 2) mixed flow with a

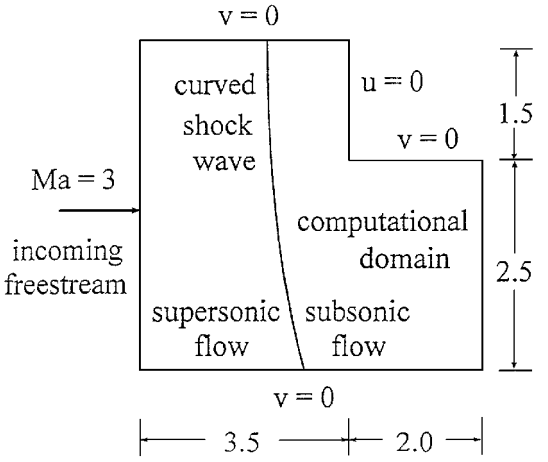

a) Domain

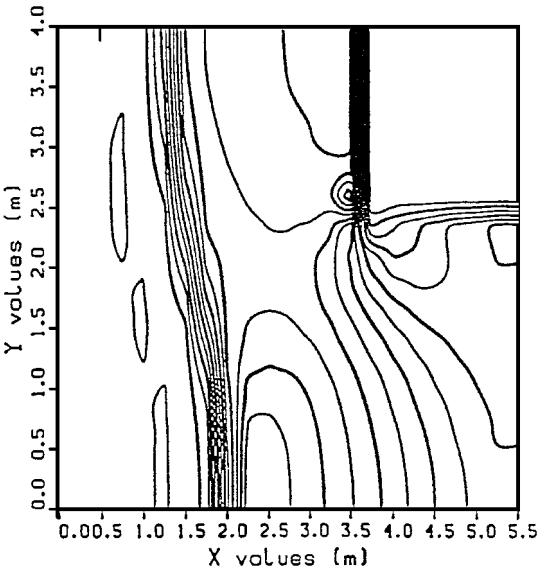

c) Pressure contour results

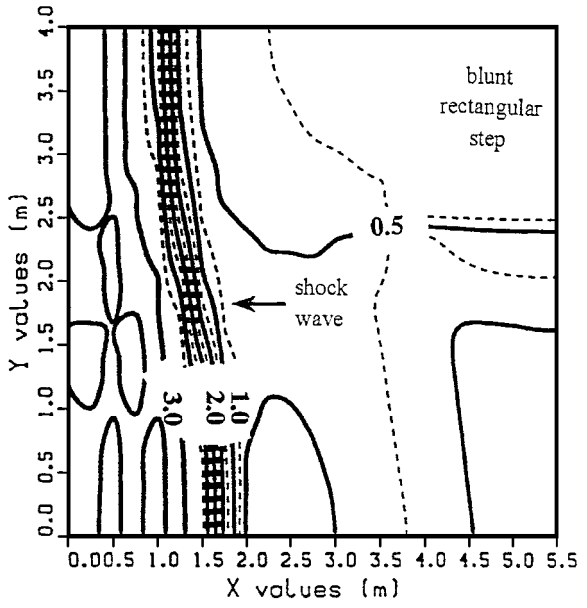

b) Mach number

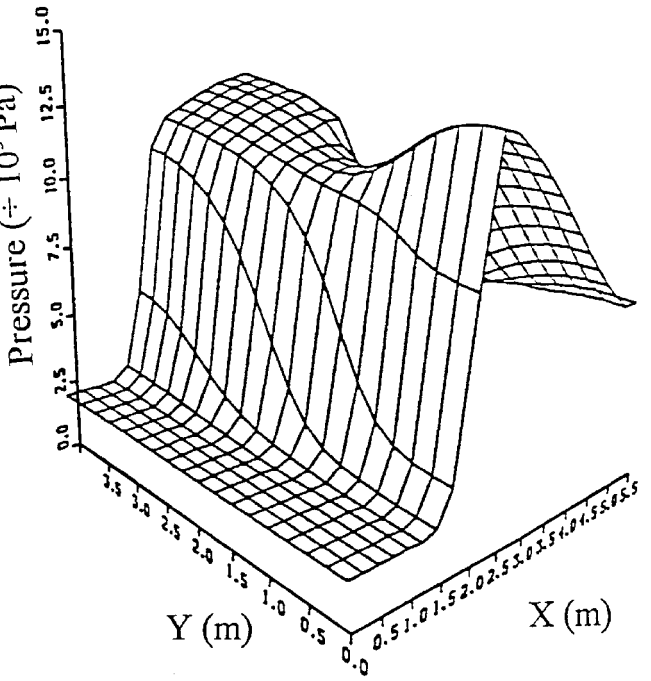

d) Pressure results: surface plot

Fig. 6 PINS two-dimensional upwinding; note that Ref. 4 develops and applies additional artificial dissipation mechanisms in a two-dimensional context.

shock wave ($P_e = 50$ kPa), and 3) supersonic flow ($P_e = 8.8$ kPa). If the back pressure is not low enough to induce sonic conditions at the throat, then the flow remains subsonic throughout the nozzle (case 1). As the back pressure is further reduced, the throat eventually becomes sonic, and the mass flux through the nozzle reaches a maximum value. If the back pressure is reduced below this critical condition, then the throat remains choked at the sonic value, and a normal shock wave occurs in the diverging section to meet the outlet condition (case 2). The design pressure ratio is achieved when the back pressure is further reduced until the diverging flow is entirely supersonic (case 3). This design condition is often used for the efficient operation of a rocket exhaust.

Comparisons between the computed and exact solutions for the mixed-flow example are shown in Fig. 4b. The computed shock-wave position is accurately predicted. Also, the sharpness of its resolution is very good because it is essentially captured over three nodes without numerical overshoots or undershoots. Numerical errors are observed with some numerical smearing downstream of the shock wave, where the fluid velocity is slightly overpredicted. If the discretization errors are examined by a truncated Taylor series expansion, then even derivative terms are typically associated with diffusion errors; these errors tend to reduce gradients in the flowfield. On the other hand, odd derivative terms are often responsible for dispersion and oscillation errors because phase relations between waves in the flowfield are distorted. The present generalized entropy approach provides a physically based alternative to Taylor series expansions for the error analysis. For example, the numerical smearing in Fig. 4b is a diffusive mechanism and, thus, an entropy-producing rather than an entropy-destroying process. The entropy-producing effect of numerical diffusion can be quantified through an equivalent diffusion coefficient in Eq. (28). Previous studies by Naterer and Schneider[4] have utilized this type of diffusion coefficient to reduce dispersion errors and to eliminate nonphysical numerical results in shock-wave predictions. The entropy-based approach also provides additional aspects of numerical stability in the computations. In particular, the numerical results converge to the unique and physically correct final solution in Fig. 4b. Further testing of this problem with different initial conditions reveals that the final

results are independent of the initial conditions. These observations suggest that the current numerical formulation satisfies the fundamental properties of entropy stability as outlined by Lax[1] and Majda and Osher,[5] among others.

For the case of supersonic flow in the diverging section, Fig. 4c shows the computed and exact temperature and Mach number results for $x \leq 5$ m (converging section). The accuracy of these computed results is also good. The Mach number increases from $Ma = 0.3$ at the inlet to a sonic and choked condition ($Ma = 1$) at the nozzle throat. The current PINS upwind scheme, i.e., $a_2 = a_3$ in Eq. (30), provides several attractive features for predicting accurate solutions. Its directional upwinding capabilities, as seen by the two-dimensional upwinding schematic in Fig. 1b, tend to reduce false diffusion errors.[14] The upwinding interpolation is also flow strength dependent, so that an appropriate balance between upstream and downstream influences, based on the local velocity magnitude, can be achieved. Its dependence on the local integration point velocity and pressure fields provides an effective enhanced grid resolution because it models the appropriate fluid flow physics at both the integration point and control volume levels. The interpolation includes all of the relevant physical influences and couplings that affect the flow variables.

A quantitative assessment of numerical accuracy and grid sensitivity has also been examined. For the flow results in the converging section, i.e., Fig. 4c, it can be observed that the resulting error in computing the temperature ratio, at various points within the nozzle, is approximately 2% at most, in comparison with the exact solution. Also, the maximum error in estimating the Mach number at various locations is approximately 2%. Differences between the computed and exact results are generally less than 1.6% at most node points. Grid refinements in the axial direction, i.e., 2×50 elements and 2×100 elements, revealed that the error levels were reduced as the number of elements increased. Also, grid refinements in the transverse direction, i.e., 2×50 elements and 4×50 elements, confirmed the quasi-one-dimensional flow character, as negligible differences between various grid results along the nozzle centerline were observed. These very accurate results, in comparison with the exact solution, suggested that the present mesh configurations were adequate for the current numerical studies. In addition, other grid sensitivity studies with the current finite element scheme have shown that the numerical error decreases approximately quadratically as grid refinement is effected.[18] In other words, second-order accuracy has been verified (see Appendix).

Figures 5a–5d show steady-state density, velocity, pressure, and temperature distributions, respectively, for the three example cases. For the entirely subsonic flow, the flow accelerates in the converging section until a point of maximum velocity and minimum pressure is reached at the throat. Then the flow decelerates in the diverging section until it reaches the prescribed outlet condition. However, in the supersonic flow example, the maximum Mach number ($Ma = 2.2$) occurs at the outlet because the flow continually accelerates through the diverging section of the nozzle to meet the prescribed outlet condition.

Two-Dimensional, Blunt-Body Impingement Problem

This problem examines supersonic flow impingement against a blunt object within a channel (Fig. 6a) to demonstrate the scheme's applicability to multidimensional problems. At the left boundary, all problem variables are set constant and equal to their initial values ($T_\infty = 300$ K, $Ma_\infty = 3.0$, and $\rho_\infty = 1.18$ kg/m^3). Along the upper and lower boundaries, zero normal velocity and zero tangential stress conditions are specified. Neumann conditions, i.e., zero normal gradient conditions, are imposed along the outflow boundary. A time step of $\Delta t = 0.02$ ms and a 358-node spatial discretization were employed in the computations. Note that the blunt step in this problem is an inactive region in the finite element mesh rather than a blocked region, which would entail further computations in typical finite difference schemes.

Figures 6b–6d show the steady-state Mach number and pressure results, respectively. The curved shock wave strikes the lower boundary, and it is captured over three to four nodes. The detached shock-wave location along the line of symmetry is approximately 1.15 step height units in front of the blunt surface, and the shock position in front of the blunt corner is approximately 1.05 step height units. These results compare well with other literature results, i.e. see Ref. 19.

In this problem, the curved sonic line ($Ma = 1$) divides the domain between the upstream supersonic region and the downstream subsonic region. Unlike the earlier example, where choked nozzle conditions limit the zone of influence, downstream disturbances, i.e., outflow boundary conditions, in this problem affect the sonic line position and the supersonic upstream structure. In the current PINS scheme, the integration point equations directly relate the nodal pressure to the local integration point velocity and, thus, the sonic line position. Therefore, a large pressure difference between adjacent nodes is accompanied by a large fluid acceleration or viscous force, i.e., shock-wave dissipation, between the shock-capturing points in Figs. 6b–6d. By improving the upwinding procedure, the PINS scheme is able to provide the analogous physical influences between pressure and velocity at the integration point that standard finite volume schemes provide at the control volume level.

Conclusions

A relationship between convection–diffusion modeling in finite volume procedures and a local form of the second law of thermodynamics has been established. Specific aspects of integration point models, such as incomplete couplings between the local velocity and pressure fields, may lead to negative production of generalized or computational entropy. However, the proposed PINS scheme provides an effective link between integration point variables that ensures a positive local entropy production rate. The local form of the second law is enforced by additional pressure and source terms in the discretized momentum transport equation. Applications to both one- and two-dimensional problems demonstrate the good accuracy and performance of the method. The role of generalized entropy in compressible flow computations has been successfully extended to the understanding of integration point approximations in finite volume methods. It forms a basis from which further developments in numerical upwinding schemes can be achieved.

Appendix: Order Accuracy

The order accuracy of the convection terms can be established by a Taylor series analysis. We must estimate the error in the approximation of ϕ at the control volume surface due to the discretization of the integration point equation. The integration point equation for an arbitrary scalar ϕ can be written in the following form:

$$\rho \mathcal{V} \phi_{,m} + \dot{\sigma} = 0 \tag{A1}$$

where the subscript $,m$ denotes differentiation in the streamwise direction, $\dot{\sigma}$ includes all transport terms except convection, and $\mathcal{V}$ is a linearized approximate integration point velocity such as the value from a previous time step. Using a skew upwind operator (see Fig. 1b),

$$\rho \mathcal{V} \left(\frac{\phi' - \phi'_u}{L} \right) + \dot{\sigma}' = 0 \tag{A2}$$

where the primes refer to inexact numerical values. Assuming that the local streamline intersects the volume edge between local nodes 2 and 3, then linear interpolation between Φ_2 and Φ_3 may be employed for the approximation of ϕ'_u:

$$\phi'_u = (a/b)\Phi_2 + [1 - (a/b)]\Phi_3 \tag{A3}$$

The order accuracy of this interpolation is determined by first forming a Taylor series expansion about the location of ϕ'_u:

$$\Phi_2 = \phi_u + (b - a)(\phi_{,n}) + \tfrac{1}{2}(b - a)^2(\phi_{,nn}) + \mathcal{O}[(b - a)^3] \tag{A4}$$

$$\Phi_3 = \phi_u - a(\phi_{,n}) + \tfrac{1}{2}a^2(\phi_{,nn}) + \mathcal{O}(a^3) \tag{A5}$$

where the local coordinate n is parallel to the element edge. Combining Eqs. (A3–A5),

$$\phi'_u = \phi_u + \mathcal{O}(b^2) \tag{A6}$$

which proves that the linear interpolation for ϕ'_u is second order. Because the integration point velocity magnitude $\mathcal{V}$ is expressed using the bilinear interpolation of the shape functions, it is also second order. Then, if the terms in $\dot{\sigma}$ are at least first order, Eq. (A2) becomes

$$\phi' = \phi_u - \frac{L\dot{\sigma} + L\mathcal{O}(L)}{\rho\mathcal{V} + \rho\mathcal{O}(L^2)} + \mathcal{O}(b^2) \tag{A7}$$

Expanding the second term on the right-hand side of Eq. (A7) by partial fractions,

$$\frac{L\dot{\sigma} + L\mathcal{O}(L)}{\rho\mathcal{V} + \rho\mathcal{O}(L^2)} = \left[\frac{L\dot{\sigma}}{\rho\mathcal{V}} - \frac{L\dot{\sigma}\mathcal{V}\mathcal{O}(L^2)}{\rho\mathcal{V}\mathcal{O}(L^2) + \rho\mathcal{V}^2}\right] + \left[\frac{\mathcal{O}(L^3)}{\rho\mathcal{V} + \rho\mathcal{O}(L^3)}\right] \tag{A8}$$

If $\mathcal{V} = \mathcal{O}(L/T)$, where T is a representative timescale for the problem, then $|\mathcal{O}(L^2)/\mathcal{V}| < 1$ as the mesh is refined. Applying a binomial expansion and combining Eqs. (A7) and (A8),

$$\phi' = \phi_u - (L\dot{\sigma}/\rho\mathcal{V}) + \mathcal{O}(b^2) + \mathcal{O}(L^2) \tag{A9}$$

Applying a Taylor series expansion about the current integration point,

$$\phi_u = \phi - L(\phi_{,m})_{\text{ip}} + (L^2/2)(\phi_{,mm})_{\text{ip}} + \mathcal{O}(L^3) \tag{A10}$$

Thus, from Eq. (A10) and the original differential equation,

$$\phi = \phi_u - (L\dot{\sigma}/\rho\mathcal{V}) + \mathcal{O}(L^2) \tag{A11}$$

Comparing this exact expression to the approximate value in Eq. (A9),

$$\phi' = \phi + \mathcal{O}(b^2) \tag{A12}$$

which proves that the integration point variable is second order.

Acknowledgments

Computational entropy aspects of the work were supported by a research grant from the Natural Sciences and Engineering Research Council of Canada to G. F. Naterer. The assistance of G. E. Schneider at the University of Waterloo, Canada, with the testing of numerical results in the initial stages of this work is appreciated.

References

[1]Lax, P. D., "Shock Waves and Entropy," *Contributions to Non-Linear Functional Analysis*, Academic, New York, 1971, pp. 603–634.

[2]Hughes, T. J. R., Franca, L. P., and Mallet, M., "A New Finite Element Formulation for Computational Fluid Dynamics: I. Symmetric Forms of the Compressible Euler and Navier–Stokes Equations and the Second Law of Thermodynamics," *Computer Methods in Applied Mechanics and Engineering*, Vol. 54, 1986, pp. 223–234.

[3]Merriam, M. L., "Smoothing and the Second Law," *Computer Methods in Applied Mechanics and Engineering*, Vol. 64, 1987, pp. 177–193.

[4]Naterer, G. F., and Schneider, G. E., "Use of the Second Law for Artificial Dissipation in Compressible Flow Discrete Analysis," *Journal of Thermophysics and Heat Transfer*, Vol. 8, No. 3, 1994, pp. 500–506.

[5]Majda, A., and Osher, S., "Numerical Viscosity and the Entropy Condition," *Communications on Pure and Applied Mathematics*, Vol. 32, 1979, pp. 797–838.

[6]Harten, A., "On the Symmetric Form of Systems of Conservation Laws with Entropy," *Journal of Computational Physics*, Vol. 49, 1983, pp. 151–164.

[7]Camberos, J. A., "Calculation of Residual Error in Explicit and Implicit Fluid Flow Simulations Based on Generalized Entropy Concept," *Proceedings of the Joint ASME/JSME Meeting*, Vol. PVP377-2, American Society of Mechanical Engineers/Japan Society of Mechanical Engineers, San Diego, CA, 1998, pp. 279–286.

[8]MacCormack, R. W., and Baldwin, B. S., "A Numerical Method for Solving the Navier–Stokes Equations with Application to Shock–Boundary-Layer Interactions," AIAA Paper 75-1, Jan. 1975.

[9]Pulliam, T. H., and Steger, J. L., "Implicit Finite Difference Simulations of Three-Dimensional Compressible Flow," *AIAA Journal*, Vol. 18, No. 2, 1980, pp. 159–167.

[10]Lohner, R., Morgan, K., and Zienkiewicz, O. C., "The Solution of the Non-Linear Hyperbolic Equation Systems by the Finite Element Method," *International Journal for Numerical Methods in Fluids*, Vol. 4, 1984, pp. 1043–1063.

[11]Karki, K. C., and Patankar, S. V., "Pressure Based Calculation Procedure for Viscous Flows at All Speeds in Arbitrary Configurations," *AIAA Journal*, Vol. 27, No. 9, 1989, pp. 1167–1174.

[12]Nellis, G. F., and Smith, J. L., "Entropy-Based Correction of Finite Difference Predictions," *Numerical Heat Transfer B*, Vol. 31, No. 2, 1997, pp. 177–194.

[13]Patankar, S. V., *Numerical Heat Transfer and Fluid Flow*, Hemisphere, New York, 1980, pp. 30, 31.

[14]Minkowycz, W. J., Sparrow, E. M., Schneider, G. E., and Pletcher, R. H., *Handbook of Numerical Heat Transfer*, Wiley, New York, 1988, pp. 252, 253.

[15]Leonard, B. P., "A Stable and Accurate Convective Modeling Procedure Based on Quadratic Upstream Interpolation," *Computer Methods in Applied Mechanics and Engineering*, Vol. 19, 1979, pp. 59–98.

[16]Schneider, G. E., and Raw, M. J., "Control-Volume Finite-Element Method for Heat Transfer and Fluid Flow Using Co-Located Variables—1. Computational Procedure," *Numerical Heat Transfer*, Vol. 11, No. 4, 1987, pp. 363–390.

[17]Fox, R. W., and McDonald, A. T., *Introduction to Fluid Mechanics*, 4th ed., Wiley, New York, 1992, pp. 123, 124.

[18]Naterer, G. F., "Subgrid Volumetric Quadrature Accuracy for Transient Compressible Flow Predictions," *International Journal for Numerical Methods in Fluids*, Vol. 25, 1997, pp. 143–149.

[19]Pepper, D., and Humphrey, J., "A Hybrid Finite Element Method for Compressible Flow," AIAA Paper 90-0399, Jan. 1990.

D. S. McRae
Associate Editor